

# Investigating unconventional superconductivity in the 2D Hubbard-Kanamori model using Functional Renormalization Group (FRG)

210003218

February-May 2025

## Contents

<b>1</b>	<b>Abstract</b>	<b>3</b>
<b>2</b>	<b>Introduction</b>	<b>3</b>
<b>3</b>	<b>Theoretical Background</b>	<b>4</b>
3.1	Unconventional superconductivity . . . . .	4
3.1.1	Spin-fluctuation mediated superconductivity . . . . .	4
3.2	Hubbard-Kanamori Model . . . . .	5
3.2.1	Tight binding Models . . . . .	5
3.2.2	Hubbard Model . . . . .	6
3.2.3	Hubbard-Kanamori Model . . . . .	6
3.3	Functional Renormalization Group (FRG) theory . . . . .	6
3.3.1	Flow equation . . . . .	7
3.3.2	Truncation scheme (TU <sup>2</sup> FRG) . . . . .	9
3.3.3	Decoupling of flow equation . . . . .	10
3.3.4	Instability calculation . . . . .	11
<b>4</b>	<b>Computational Methods</b>	<b>11</b>
4.1	divERGE . . . . .	11
4.2	Convergence of Calculation . . . . .	12
4.2.1	Form factor convergence . . . . .	12
4.2.2	Convergence with number of k points . . . . .	13
<b>5</b>	<b>Results and discussion</b>	<b>13</b>
5.1	Nearest-neighbour 2D Hubbard Model on a square lattice (1NN) . . . . .	14
5.1.1	Superconductivity in the 1NN Model . . . . .	16
5.1.2	Magnetic stripes in the 1NN Model . . . . .	17
5.2	Effect of next-nearest neighbour hopping (1NNN model) . . . . .	18

5.2.1	Superconductivity in the 1NNN Model . . . . .	18
5.2.2	Magnetic stripes in the 1NNN model . . . . .	21
5.2.3	Continuous variation of next-nearest neighbour hopping . . . . .	21
5.3	Effect of bi-orbital system (1NN2 model) . . . . .	22
<b>6</b>	<b>Conclusion and Outlook</b>	<b>25</b>
<b>A</b>	<b>Appendix A</b>	<b>30</b>

# 1 Abstract

The two-dimensional Hubbard model has attracted sustained scientific interest for decades, largely because of its ability to capture most of the underlying physics of the superconducting phase of the high-temperature cuprate superconductors [1]. Beyond its relevance to the Cuprates, it also serves as a fundamental toy model in theoretical physics. This thesis conducts a detailed analysis of the 2D Hubbard model using the truncated-unity functional Renormalization Group (TU<sup>2</sup>FRG) method, within the framework of spin-fluctuation-mediated superconductivity. The interplay between magnetism and superconductivity is explored by systematically varying model parameters such as the on-site Coulomb repulsion, chemical potential, Hund’s coupling, next-nearest-neighbor hopping, and the number of orbitals per site. This approach enables the identification of clear trends in the superconducting critical ( $T_c$ ) temperature and order parameter, while also providing insights into the magnetic ordering and how well FRG works for a certain range of parameters.

## 2 Introduction

Since its discovery in 1911 [2], superconductivity has remained a topic of great scientific interest. This phenomenon, characterised by an abrupt drop in resistance at a so-called “Critical Temperature ( $T_c$ )” [3] is driven by an attractive interaction between electrons. This interaction leads to the formation of electron pairs, famously known as “Cooper pairs” [4]. For many years after the discovery of superconductivity, physicists were convinced that BCS-Eliashberg-electron-phonon theory [4] provided a complete explanation of the electron pairing mechanism in all superconducting materials. However, in 1979, the discovery of the first heavy-fermion superconductor [5] gave rise to a whole new class of materials: Unconventional Superconductors. These are condensates of cooper pairs formed by a different pairing mechanism than the electron-phonon coupling predicted by BCS theory [6]. For many materials, there is no consensus on what the mechanism otherwise is.

High-temperature superconductors are a special class of unconventional superconductors. They are defined by having a critical temperature greater than the boiling point of Nitrogen (77K). Ever since the discovery of the first high- $T_c$  superconductor [7], the search for “(close to-) room temperature” superconductors has been extended to all kinds of unconventional superconductors. However, a comprehensive understanding of what drives the superconductivity is required in order to achieve this. There have been multiple attempts to model the pairing mechanism of some families of high- $T_c$  superconductors, most of which have been greatly limited by the numerical challenges that working with complex lattice structures present.

Motivated by these challenges and by the need for simplified yet insightful models, this work turns to the two-dimensional Hubbard model-one of the most fundamental frameworks in condensed matter physics. Truncate Unity Functional Renormalisation Group (TU<sup>2</sup>FRG) [8] is employed to investigate the influence of the Coulomb repulsion ( $U$ ) and chemical potential ( $\mu$ ) on the interplay between magnetism and superconductivity. This is done under the key assumption that superconductivity arises from spin-fluctuation mediation. In this work, regions of stable magnetic and superconducting order are identified, and trends in their respective ordering and

critical temperatures are presented. The study is further extended by examining how variations in the next-nearest-neighbor hopping amplitude and the inclusion of a second orbital per site impact all the above.

## 3 Theoretical Background

### 3.1 Unconventional superconductivity

Most generally, the Hamiltonian for a superconducting state can be described as follows:

$$\hat{H} = \hat{H}^0 + \hat{H}^{cp} \quad (1)$$

where  $\hat{H}^{cp}$  describes the pairing interaction that leads to the formation of a Cooper pair and is given by:

$$\hat{H}^{cp} = \sum_{k,k'} \Gamma(k, k') c_{k,\uparrow}^\dagger c_{k',\downarrow}^\dagger c_{k',\uparrow} c_{-k,\downarrow} \quad (2)$$

In s-wave symmetric superconductors, the effective pairing interaction  $\Gamma(k, k')$  is momentum-independent and thus remains constant. For many unconventional superconductors-including those with spin-fluctuation mediated pairing-the exact form of  $\Gamma(k, k')$  has remained as an unanswered question for decades.

#### 3.1.1 Spin-fluctuation mediated superconductivity

The prevailing assumption for the pairing mechanism in Iron-based or heavy-fermion compounds is that it is driven by spin fluctuations [9]. This section discusses how to model spin-fluctuation mediated superconductivity for the fluctuation-exchange approximation (FLEX) [10].

In such cases, the effective pairing interaction  $\Gamma(k, k')$  is given by <sup>1</sup>:

$$\Gamma(k, k') = \frac{3}{2}U^2\chi^S(k - k') - \frac{1}{2}U^2\chi^C(k - k') + U \quad (3)$$

This equation is taken from [11]. Here,  $U$  is the on-site Coulomb repulsion and  $\chi^S$ ,  $\chi^C$  are the interacting spin-susceptibilities in the Charge (C) and Spin(S) channel respectively. Their form is given below.

$$\chi^S(q) = \frac{\chi^0(q)}{1 - U\chi^0(q)} \quad (4)$$

$$\chi^C(q) = \frac{\chi^0(q)}{1 + U\chi^0(q)} \quad (5)$$

These interacting spin susceptibilities are expressed in terms of the non-interacting dynamic spin susceptibility ( $\chi_{ps}^0$ ) [9], stated below:

---

<sup>1</sup>Note that this form of pairing interaction assumes that the ratio between the fluctuation frequency ( $w_f$ ) and the Fermi energy is small.

$$\chi_{ps}^0(q, i\omega) = - \sum_k \int_0^\beta d\tau G_{ps}^0(k + q\tau) G_{sp}^0(k, -\tau) e^{i\omega\tau} \quad (6)$$

The calculations presented in this project are carried out in the spin-fluctuation framework. Whilst this theory has managed to successfully capture key features in the phase diagrams of unconventional superconductors, it also has its limitations. The most relevant example is that of the Cuprate phase diagram: spin-fluctuation theory is able to capture the superconducting dome and the correct order parameter [12, 13] but fails to describe the characteristic pseudo-gap and Mott insulating phase [14].

## 3.2 Hubbard-Kanamori Model

### 3.2.1 Tight binding Models

The Tight Binding Model is a central element of condensed matter physics (7). In this model, electrons are bound in orbitals around the lattice ions. Due to the overlap between the quantum mechanical wave-functions that describe these orbitals, electrons are allowed to 'hop' to neighbouring sites. The probability that this hopping process will occur is given by a tunnelling amplitude, which can be calculated using a hopping integral.

This work is carried out in the tight-binding framework, where the magnitude of the tunnelling amplitudes is at first treated as a free parameter. The starting point is a simple nearest-neighbour hopping tight binding model. The effect of introducing a next-nearest-neighbour hopping and an extra orbital per site is then investigated (*See Fig. 1*).

$$\hat{H}_{TB}(\mathbf{R}) = \sum_{ij\sigma} t_{ij} (\hat{c}_{i\sigma}^\dagger \hat{c}_{j\sigma} + h.c) \quad (7)$$

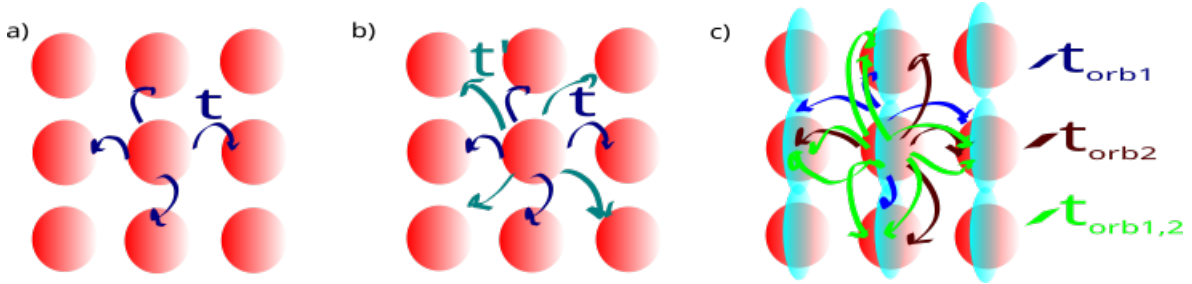


**Figure 1: Two-Dimensional Tight-Binding Models:** Three panels showing the tight binding models for the 1NN, 1NNN and 1NN2 models discussed in Section 5.1, 5.2 and 5.3 respectively. Panel a) shows the nearest-neighbour hopping case, where  $t$  depicts the hopping amplitude between the neighbouring sites. Panel b) shows the inclusion of the next-nearest neighbour hopping, the magnitude given by  $t'$ . Panel c) Shows the extension to the two-orbital case, depicting same orbital ( $t_{orb1}$ ,  $t_{orb2}$ ) and different orbital ( $t_{orb1,2}$ ) nearest-neighbour hopping. Note that this is just a pictorial representation of the orbitals, and that it does not correspond to a particular choice of orbitals or their real space projection.

### 3.2.2 Hubbard Model

The tight binding model as defined above fails to account for any interactions between electrons. This motivates the extension of this model to the Hubbard model (8), which includes the (onsite) Coulomb repulsion between electrons. Despite its simple form, this model can describe very rich physical phenomena. In particular, it becomes very interesting to study when the Coulomb repulsion ( $U$ ) and the nearest neighbour hopping ( $t$ ) are of comparable order, since it highlights the competing phenomena that take place in correlated systems. The 2D Hubbard model is able to predict all sorts of correlated phases: it describes metals, insulators, superconductors and other exotic phases [15–18]. This model has been widely studied since it resembles the structure of the Cuprate high-temperature superconductors [1].

$$\hat{H} = \sum_{ij\sigma} -t_{ij}(\hat{c}_{i\sigma}^\dagger \hat{c}_{j\sigma} + h.c.) + U \sum_i \hat{n}_{i\uparrow} \hat{n}_{i\downarrow} \quad (8)$$

### 3.2.3 Hubbard-Kanamori Model

In the case of materials with a multi-band and/or multi-orbital nature, the Hubbard model is not sufficient to capture all physical phenomena. This motivates the extension of the Hubbard model to the Hubbard-Kanamori model [19] by including a Hund's coupling term.

$$H_{int} = U \sum_{is} n_{i,s\uparrow} n_{i,s\downarrow} + \frac{V}{2} \sum_{i,s,t \neq s} n_{is} n_{it} - \frac{J}{2} \sum_{i,s,t \neq s} \vec{S}_{is} \cdot \vec{S}_{it} + \frac{J'}{2} \sum_{i,s,t \neq s} \sum_{\sigma} c_{is\sigma}^\dagger c_{is\bar{\sigma}}^\dagger c_{it\bar{\sigma}} c_{it\sigma} \quad (9)$$

Here,  $U$  and  $V$  represent the electronic interactions in the same and different orbitals respectively. For generality, the intraorbital exchange  $J$  and the 'pair hopping' term  $J'$  following from Hund's rule coupling have been separated. Note that this Hamiltonian is relevant for the later section of this project, where the model is extended to a two-orbital, two-dimensional Hubbard model.

## 3.3 Functional Renormalization Group (FRG) theory

Solving the Hubbard-Kanamori Hamiltonian is rather challenging, which is why one resorts to numerical techniques such as FRG. This technique falls into the same category of many other weak-coupling methods (such as mean field-theory [20], perturbation theory [21], Density Functional theory [22] or the Random Phase approximation [23]). In these theories, interactions between electrons are considered to be weak. This allows one to effectively model the electrons in the system as free particles and treat their interactions as a perturbation. In the non-interacting limit, the method is therefore exact. Beyond this limit, the method's precision is controlled by the ratio between the interaction strength and the bandwidth of the system.

The behavior of interacting electrons is strongly influenced by the energy scale. In the FRG approach, the degrees of freedom corresponding to different energy scales are treated successively, progressing step-by-step from higher to lower energies. Metaphorically, FRG functions like a microscope with adjustable resolution: one begins with a detailed, high-resolution view of the

fundamental microscopic laws and gradually lowers the resolution to arrive at a coarse-grained description of macroscopic collective phenomena.

In this section the theoretical framework for FRG calculations is outlined. The central element of FRG is a flow equation that describes the evolution of the effective action of the system with respect to a scalar/flow parameter Lambda ( $\Lambda$ ) (*See section 3.3.1*). The flow equation can be solved exactly for a limited number of systems, so in most scenarios an approximation has to be made in order to reach a solution in a reasonable computational time. This is where the TU<sup>2</sup>FRG scheme comes into play. TU<sup>2</sup>FRG only considers two-particle interactions and neglects any higher order terms. This allows the separation of the effective action of the system into three terms. Each term represents one of the following three physical channels: Superconductivity, Spin-Density and Charge-Density Waves<sup>2</sup>. The calculation is then performed to determine the first to diverge, this will correspond to the respective physical ground state that the model exhibits. This rather conceptual overview of FRG (and in particular the TU<sup>2</sup>FRG scheme) is represented in a flowchart below (*See Fig.2*).

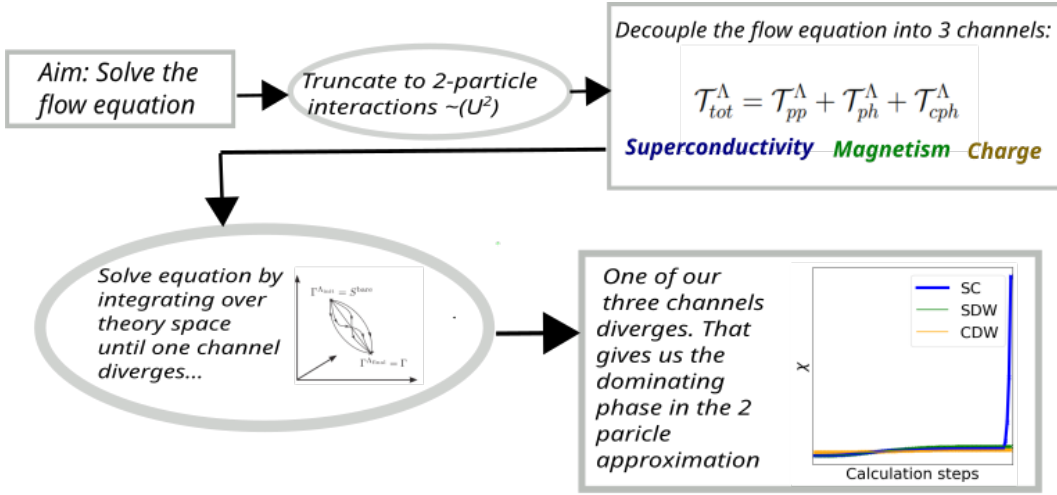


Figure 2: **FRG Flowchart:** Schematic illustration of the TU<sup>2</sup>FRG calculation process. The procedure begins by truncating the flow equation to two-particle interactions. This allows for the separation of the effective action into three distinct “physical” channels. Each channel is then computed independently, and the dominant phase is identified as the one in which the corresponding channel diverges.

### 3.3.1 Flow equation

In this section the derivation of the flow equation is outlined. If interested in the finer details of the derivation, the reader is referred to [24].

<sup>2</sup>The concept of charge density wave and spin density wave remains distinct and well-defined as long as spin-orbit coupling is not present

The central elements of statistical physics are the partition function, the canonical potential and its Legendre transformations. These are such powerful physical quantities that one can derive all physical observables from them. For quantum many-body problems, one works instead with the partition functional, defined as follows in Eq.10:

$$\mathcal{Z}[\bar{\eta}, \eta] = \int \mathcal{D}\bar{\psi} \mathcal{D}\psi e^{\mathcal{S}[\bar{\psi}, \psi]} e^{(\bar{\eta}, \psi) + (\eta, \bar{\psi})} \quad (10)$$

In the case of fermionic systems, the action in the exponent of Eq.10 takes the form shown below.

$$\mathcal{S}[\psi, \bar{\psi}] = -(\bar{\psi}, G_0^{-1} \psi) + V[\psi, \bar{\psi}] \quad (11)$$

Here,  $V[\psi, \bar{\psi}]$  is an arbitrary many-body interaction and  $G_0$  represents the propagator of the non-interacting system. This equation contains the shorthand notation “(...)”, which represents the sum  $\sum_x \bar{\psi}(x)(G_0^{-1}\psi)(x)$ ,  $(G_0^{-1}\psi)(x) = \sum_{x'} G_0^{-1}(x, x')\psi(x')$ . In this sum, the Grassman field index  $x$  encodes all the quantum numbers of the single-particle basis and imaginary time.

Note that in the limiting case where  $V = 0$ , the path integral in Eq.10 is exactly solvable. However, the situation becomes considerably more intricate when electronic correlations are taken into account. The main idea behind FRG is to introduce a cut-off in the non-interacting Green’s function ( $G_0 \rightarrow G_0^\lambda = f(\lambda)G_0$ ). This cutoff is then interpolated between the solvable initial state and the full path integral solution by subsequently including electronic interactions. For a spin-independent system this would transform the bare propagator as shown in Equations (12) and (13).

$$G_0(k_0, \mathbf{k}) \rightarrow G_0^\lambda(k_0, \mathbf{k}) \quad (12)$$

$$\frac{1}{ik_0 - \xi_{\mathbf{k}}} \rightarrow \frac{\theta^{\mathbf{k}}}{ik_0 - \xi_{\mathbf{k}}} \quad (13)$$

where  $\theta^\lambda(\mathbf{k})$  is defined, for example, as follows:

$$\theta^\lambda(\mathbf{k}) = \Theta(|\xi_{\mathbf{k}}| - \lambda) \quad (14)$$

With this particular choice of cutoff scheme, the calculation then excludes points close to the Fermi Surface (*See Fig.3*).

In the following steps the derivation will proceed in the framework of the so-called “effective action”<sup>3</sup> ( $\mathcal{T}[\psi, \bar{\psi}]$ ). This is the Legendre transformation of the Greens function functional ( $\mathcal{G}[\eta, \bar{\eta}]$ ), defined below in Equations (17) and (15, 16) respectively.

$$\mathcal{G}[\eta, \bar{\eta}] = -\ln(\mathcal{Z}[\eta, \bar{\eta}]) \quad (15)$$

$$\mathcal{G}[\eta, \bar{\eta}] = -\ln \int \mathcal{D}\psi \mathcal{D}\bar{\psi} e^{-\mathcal{S}[\psi, \bar{\psi}]} e^{(\bar{\eta}, \psi) + (\bar{\psi}, \eta)} \quad (16)$$

---

<sup>3</sup>If interested in why see Ref. [24]



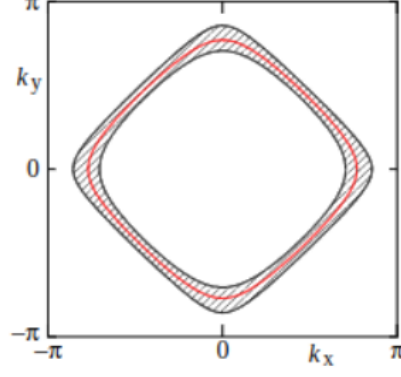


Figure 3: **Cut-off scheme example:** Momentum space region (shaded in grey) around the Fermi-surface (red) that is excluded by a momentum cut-off for a 2D square lattice. Taken from [24].

$$\mathcal{T}[\psi, \bar{\psi}] = (\bar{\eta}, \psi) + (\bar{\psi}, \eta) + \mathcal{G}[\eta, \bar{\eta}] \quad (17)$$

The next step is to introduce a scalar flow parameter ( $\lambda$ ) into the generating functionals defined above. This is done in the same manner as outlined in the example shown in Equations 12 & 13. But, more generally, this has to be performed such that the generators recover their original structure at  $\lambda = 0$ . After a series of algebraic manipulations, which are omitted here but can be found in [24], one arrives at the exact functional flow equation for the effective action:

$$\frac{d}{d\lambda} \mathcal{T}^\lambda[\psi, \bar{\psi}] = (\bar{\psi}, \dot{Q}_0^\lambda \psi) - \frac{1}{2} \text{tr}(\dot{Q}_0^\lambda (\Gamma^{(2)\lambda}[\psi, \bar{\psi}])^{-1}). \quad (18)$$

Where  $\Gamma^{(2)\lambda}[\psi, \bar{\psi}]$  and  $\mathbf{Q}_0^\lambda$  are given by equations (19) and (20) respectively.

$$\Gamma^{(2)\lambda}[\psi, \bar{\psi}] = \begin{bmatrix} \bar{\delta} \delta \Gamma[\psi, \bar{\psi}](x', x) & \bar{\delta} \bar{\delta} \Gamma[\psi, \bar{\psi}](x', x) \\ \delta \delta \Gamma[\psi, \bar{\psi}](x', x) & \delta \bar{\delta} \Gamma[\psi, \bar{\psi}](x', x) \end{bmatrix} \quad (19)$$

$$\mathbf{Q}_0^\lambda = \begin{bmatrix} Q_0^\lambda & 0 \\ 0 & -Q_0^{\lambda t} \end{bmatrix} = \text{diag}(Q_0^\lambda, -Q_0^{\lambda t}), \quad (20)$$

$\Gamma^{(2)\lambda}$  and  $\mathbf{Q}_0^\lambda$  are given by the reciprocal of the Green's and non-interacting Green's function respectively. The key point is that the Flow equation is well-defined. This flow equation is the central element of FRG and the sections below outline how to solve it.

### 3.3.2 Truncation scheme (TU<sup>2</sup>FRG)

The flow equation derived above can be solved exactly only for a small class of systems; for most models, Functional Renormalisation Group (FRG) calculations are highly computationally expensive. In order to tackle this issue, the truncated unity approximation (TU<sup>2</sup>FRG) was introduced in 2017 [25] and later improved in 2020 [8]. The main idea behind this scheme is to find a new basis that, with a controlled loss of accuracy, can represent all required elements in a

compressed way. It can be shown that such a basis can be constructed and is well-defined in the case where the calculation is constrained to terms in the order of  $U^2$  (*two-particle interactions*) [26]. Partitions of unity <sup>4</sup> are then introduced into a specific part of the flow equation. This reduces an otherwise computationally expensive nested integral to a matrix product.

Whilst the truncated scheme presents advantages in computational efficiency, particularly for lattice models with broken translational symmetry, it also has its limitations.  $TU^2FRG$  relies on short-range interactions, thus struggling to capture strongly correlated phases. This is particularly relevant for the study of the 2D Hubbard model.  $TU^2FRG$  will not be able to capture the characteristic Mott insulating phase of the Cuprate phase diagrams [27], which limits how well the results presented in this project can be directly compared with existing literature. More importantly, the truncation scheme has a direct consequence on the accuracy of the predicted phase transition temperature ( $T_c$ ). Whilst it is able to correctly capture the trends in  $T_c$ , the values predicted are much higher than what is reasonable to expect in real materials (*These unphysically large values are expected to decrease if higher order particle interactions are included*). Nevertheless,  $TU^2FRG$  successfully captures the competition between magnetic and superconducting instabilities, a central focus of the results presented in this project.

### 3.3.3 Decoupling of flow equation

After constraining ourselves to the case of two-particle interactions in the framework of translationally invariant systems, one can decouple the two-particle coupling as a function of the flow parameter ( $\lambda$ ) into three channels:

$$V(k_1, k_2, k_3, k_4) = V_{k_1, k_2, k_3, k_4}^{(0)} - \phi_{k_1+k_2, \frac{k_1-k_2}{2}, \frac{k_4-k_3}{2}}^P + \phi_{k_1-k_3, \frac{k_1+k_3}{2}, \frac{k_2+k_4}{2}}^C + \phi_{k_3-k_2, \frac{k_1+k_4}{2}, \frac{k_2+k_3}{2}}^D \quad (21)$$

Here, the three channels correspond to a particle-particle, crossed particle-hole and (three) direct particle-hole terms. These are strongly related to their respective effective actions (22-24). They represent all possible ways in which two particles can interact in the correlated system. The particle-particle (P), cross-particle-hole (C) and direct-particle-hole (D) channels correspond to the Superconducting, Charge and Magnetic phases respectively.

$$\dot{\phi}_{k_1+k_2, \frac{k_1-k_2}{2}, \frac{k_4-k_3}{2}}^P = -\mathcal{T}_{pp}(k_1, k_2, k_3) \quad (22)$$

$$\dot{\phi}_{k_1-k_3, \frac{k_1+k_3}{2}, \frac{k_2+k_4}{2}}^C = -\mathcal{T}_{cr-ph}(k_1, k_2, k_3) \quad (23)$$

$$\dot{\phi}_{k_3-k_2, \frac{k_1+k_4}{2}, \frac{k_2+k_3}{2}}^D = -\mathcal{T}_{d-ph}(k_1, k_2, k_3) \quad (24)$$

The decoupling outlined above enables the treatment of the effective action as a separable object:

$$\mathcal{T}[\psi, \bar{\psi}] = \mathcal{T}_{pp}[\psi, \bar{\psi}] + \mathcal{T}_{ph}[\psi, \bar{\psi}] + \mathcal{T}_{cph}[\psi, \bar{\psi}] \quad (25)$$

---

<sup>4</sup>These can be essentially regarded as delta functions in momentum and real space. Their exact form can be found in [26].

### 3.3.4 Instability calculation

This section provides an outline of the procedure following the decoupling the effective action and flow equation, for more details the reader is referred to [28]. In the TU<sup>2</sup>FRG method, the resulting decoupled flow equation is solved through nested integration, involving both a coarse momentum integration and a refined integration around each  $k$  point. This calculation yields the self-energy and the two particle vertex<sup>5</sup>. Although these quantities are not directly measurable, they serve as the foundation for further analysis. The first post-processing step involves identifying which of the three interaction channels diverges, revealing the leading susceptibility. Mean-field analysis [29] is then performed at the critical scale in order to determine the ordering symmetry and derive a linearized gap equation for the superconducting channel<sup>6</sup> (*See equation 26*) [28]. From this one can compute the superconducting gap and order parameter.

$$\Delta = aF(GG)|_{\Delta=0}\Delta \quad (26)$$

## 4 Computational Methods

After having discussed the required theoretical background, the implementation of the necessary concepts within the framework of this project is now addressed. The primary goal is to obtain a computational solution for the 2D Hubbard-(Kanamori) model, utilizing the divERGE package. This package implements the TU<sup>2</sup>FRG formalism discussed in Section 3.3.2. All calculations are conducted within the framework of spin-fluctuation mediated superconductivity (*see Section 3.1.1*), focusing solely on electronic interactions and neglecting other instabilities, such as lattice instabilities (e.g. charge density waves or phonon-mediated superconductivity). This section provides an overview of the divERGE package, together with the convergence tests required to ensure the accuracy of the results.

### 4.1 divERGE

divERGE is an open-source, high-performance, C/C++/Python library that includes a truncated unity FRG (TU<sup>2</sup>FRG) computational backend [30]. At the core of the truncated-unity calculation is a model that incorporates all the essential physical parameters. This model must accurately reflect the system’s kinematics, based on its real-space hopping parameters. It is equally important to define structural details such as the Bravais lattice vectors, the number of atoms per unit cell, and the number of orbitals per atom. Once the model is established, six input parameters must be specified for the calculation to proceed: the strengths of the Coulomb repulsion ( $U$ ) and Hund’s coupling ( $J$ ), the value of the chemical potential ( $\mu$ ), as well as the form factor cut-off,  $n_k$  and  $n_{k_f}$  values. (*The latter three terms are depicted in Fig.4 and discussed in more detail in Section 4.2*).

---

<sup>5</sup>For precise definitions of these quantities, see [24].

<sup>6</sup>The equation here is expressed in terms of the Greens functional  $G$  and vertex function  $F$ . Note that this form of linearised gap equation is valid for a small gap magnitude.

With the model constructed, and all necessary parameters defined, the calculation can proceed. Under the approximations described in Section 3.3.2, the flow equations are integrated numerically from high energy scales ( $\lambda = \infty$ ) down to low scales ( $\lambda = 0$ ), by incrementally stepping from  $\lambda$  to  $\lambda + d\lambda$ . This integration continues until a phase transition is detected-signaled by the divergence of one of the interaction channels-or until  $\lambda$  is smaller than  $1e - 6$  eV<sup>7</sup>. In the latter case, the system is considered to remain in a Fermi-liquid state. All such computations were performed on the high-performance computing (HPC) cluster at the University of St Andrews.

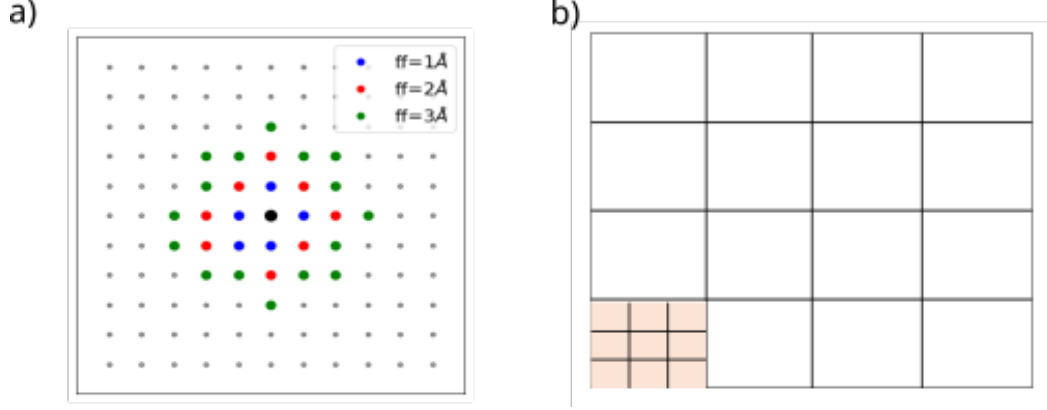


Figure 4: **Pictorial depictions of the form factor-cutoff,  $n_k$  and  $n_{k_f}$ :** *Panel a)* Form factor cut-off for a 2D square lattice. Increasing the form factor cut-off from 1-3Å increases the number of additional bonds that are included in a calculation for a given site. *Panel b)* A 3x4  $n_k \times n_{k_f}$  integration grid.  $n_k$  represents the number of k points used for the general momentum integral. In turn,  $n_{k_f}$  represents the number of k points for an additional momentum integral around each point. The outer loop is a 3x3 grid, which refined by a factor of 4 becomes a 12x12 grid.

## 4.2 Convergence of Calculation

In the truncated-unity approximation, several convergence tests must be performed to ensure that calculations are accurate. These tests include checking the form factor convergence and the number of  $k$  points.

### 4.2.1 Form factor convergence

The set of orthogonal basis functions ( $f_m$ ) used to describe the truncated space (*See section 3.3.2*) in momentum representation is called the form factor basis [26]. In the case of the square lattice, the form factors take the form of delta functions in real space; they are arranged as circles with increasing radii around the origin. This effectively leads to a “bond-like” representation where the form-factor cut-off represents how many of the neighbouring bonds are accounted for in the calculation of each point in the phase diagram (*See Fig.4a*).

---

<sup>7</sup>This corresponds to about 0.1K.

The divERGE package allows the user to modify the form-factor cutoff accordingly. Choosing appropriate values ultimately comes down to a trade-off between computational accuracy and expensiveness. For the results in this project, the form factor value was set at  $4\text{\AA}^8$  after the convergence of the calculations was tested accordingly for a range of points in the phase diagram (*an example of such tests is shown in Fig.5*). Moreover, this value is in agreement with values used in previous literature [26].

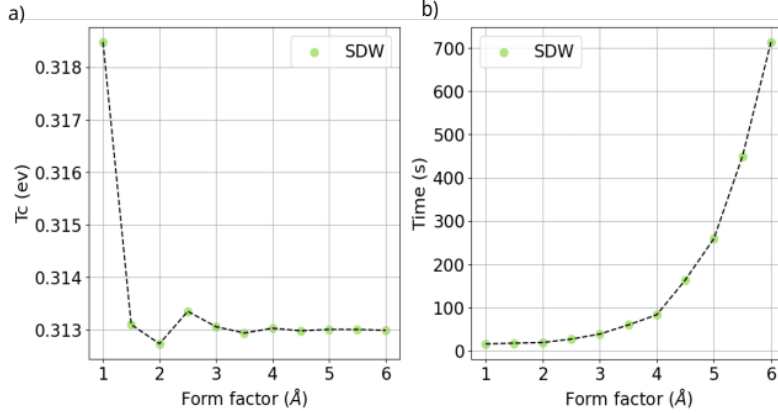


Figure 5: **Convergence testing:** Panel a) Transition temperature as a function of form factor for the nearest-neighbour 2D Hubbard model,  $U = 5.00$ ,  $\mu = 0.20\text{eV}$ . Panel b) Time taken to complete the calculation as a function of form factor.

#### 4.2.2 Convergence with number of k points

When integrating the flow equation, there are two parameters that can be further tuned to ensure convergence. These are the  $n_k$  and  $n_{k_f}$  values, and they specify the number of k points used to carry out the nested integration of the decoupled flow equation. In particular,  $n_k$  refers to the number of k points used for the general momentum integral, and  $n_{k_f}$  to the number of k points used for the additional sum around each k-point *See Fig.4b*. The calculations performed here were carried out with an integration grid of  $20 \times 5$  ( $n_k \times n_{k_f}$ ) points. This means that the outer calculation is therefore a  $20 \times 20$  grid, the inner loop is refined by a factor of 5 and is a  $100 \times 100$  grid. The choice of parameters ensured that the calculations had converged appropriately and resulted in an average computational time of  $\approx 180\text{s}$  per point for the simpler models<sup>9</sup>.

## 5 Results and discussion

The findings of this project are presented across three sections, each dedicated to a different model: the nearest-neighbour, next-nearest-neighbour and nearest-neighbour bi-orbital 2D Hubbard model on a square lattice (*See Fig.1*). These sections explore the interplay between mag-

<sup>8</sup>This is equivalent to a number of form factor shells of 4 since the lattice spacing of the models here is set to  $1\text{\AA}$ .

<sup>9</sup>Note that the computational time increases as a function of Coulomb repulsion  $U$ .

netism and superconductivity, highlighting trends in the superconducting order parameter and spin density wave ordering vectors. Additionally, they investigate how variations in parameters such as Coulomb repulsion, chemical potential, Hund's coupling, next-nearest-neighbor hopping, and the number of orbitals per site influence the critical temperature of the superconducting regions.

## 5.1 Nearest-neighbour 2D Hubbard Model on a square lattice (1NN)

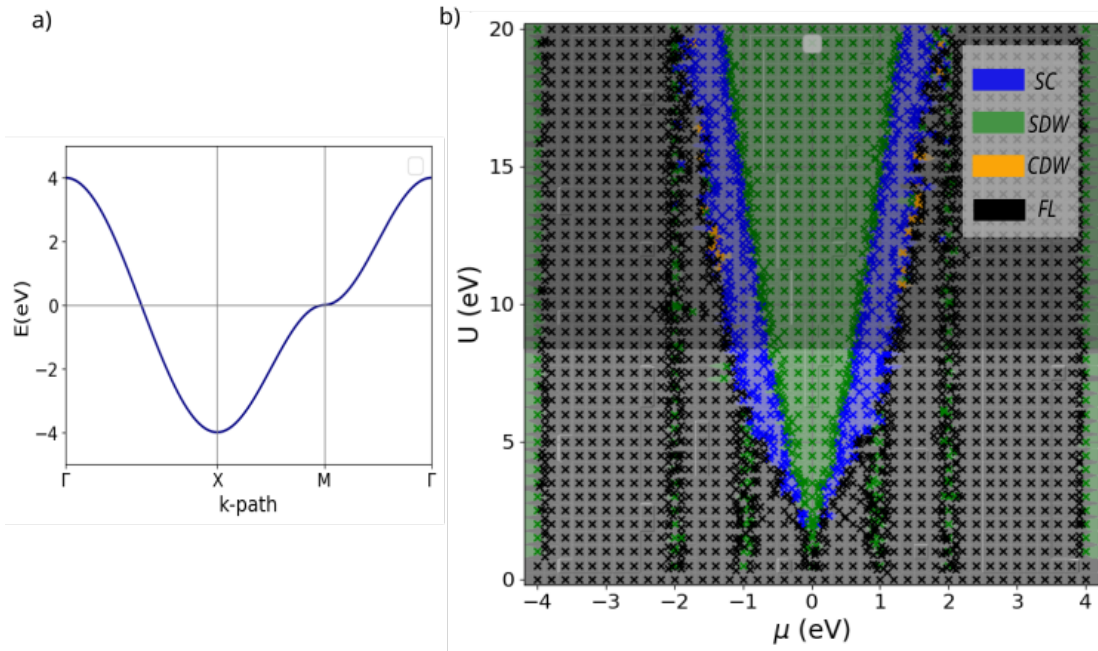


Figure 6: **Nearest neighbour 2D Hubbard model on a square lattice:** Panel a) Band structure for the undoped nearest neighbour 2D Hubbard model on a square lattice. Panel b) Phase diagram as a function of Coulomb repulsion  $U$  and chemical potential  $\mu$ . The phase diagram shows four phases: SC (Superconductivity), SDW (Spin-Density Wave), CDW (Charge Density Wave) and FL (Fermi-Liquid). Calculated points are shown by an 'x' marker; lighter coloured regions show the interpolated regions between these points. A darker mask is applied for  $U > 8$  eV to show the region where results become unphysical.

The 1NN model is defined as the 2D Hubbard model on a square lattice with a single orbital per site, allowing hopping between nearest-neighbour sites (*a diagrammatic representation can be found in Fig.1.a*). In this project the 1NN model is constructed by setting the nearest-neighbour hopping parameter to 1eV. Fig.6a shows the band structure of the model along the high-symmetry

points  $\Gamma - X - M - \Gamma$  (which correspond to a momentum path of  $(0, 0) - (\pi, 0) - (\pi, \pi) - (0, 0)$  along the square lattice). The model has a bandwidth of 8 eV and exhibits a Van-Hove singularity (singularity in the density of states) at the  $M$  symmetry point  $(\pi, \pi)$ .

As discussed in Section 3.2.2, solving this model near half-filling presents significant challenges. This section investigates the solution to the 1NN Model Hamiltonian using two-particle interaction-truncated FRG. A phase diagram, plotted in terms of the on-site Coulomb repulsion  $U$  and chemical potential  $\mu$  is presented and analyzed in detail. While previous FRG studies on the 2D Hubbard model exist [31–33], they mostly focus on specific regions of the phase diagram. As a result, there has been limited investigation into the effects of varying the on-site Coulomb repulsion. The present work explores a much broader range of parameters than what has been previously studied: Coulomb repulsion values ranging from 1-20 eV and chemical potential values spanning the entire bandwidth of the model (from -4 eV to 4e V).

Before diving into the results, it is important to be aware of several caveats. In real materials, the chemical potential is a tuneable parameter due to its strong connection to the electronic doping of the system. In turn, controlling the magnitude of the Coulomb repulsion between electrons is far from straightforward. Additionally, some interesting features discussed in this report fall outside the physical regime—specifically, the FRG calculation assumes a weak-coupling limit, meaning that any Coulomb repulsion values exceeding the bandwidth of the material (8 eV) are unphysical in this context. Whilst unphysical, calculating these values is nevertheless insightful. It allows for further understanding of the behaviour of FRG on electronic structure models, identifying the strengths and limitations of the technique. The primary goal in this project is to understand how variations in certain parameters ( $U$ ,  $\mu$ ,  $t'$ ) influence the correlated phases observed in the model. Finally, it is also important to note, as discussed in Section 3.3.2, that any analysis of the superconducting transition temperature should be treated qualitatively (*at no point does this work claim to have identified superconducting regions with transition temperatures of the order of thousands of Kelvin*).

The complete phase diagram for the values discussed above is shown in Fig.6. As is expected for both the Hubbard model and the Cuprates [34–36], a pronounced competition between Magnetism and Superconductivity (SC) is observed. This interplay gives rise to a prominent magnetic dome, sandwiched between two narrower d-wave superconducting regions. This magnetic dome is anti-ferromagnetically (AFM) ordered and its width increases with increasing Coulomb repulsion is increased. In other words, a stronger Coulomb repulsion favours the magnetic instability as the “leading ground state” of this magnetism/SC competition for a larger range of doping values. Both AFM and d-wave SC arise from repulsive scattering between  $(\pi, 0)$  and  $(0, \pi)$  vectors. Therefore, their competition peaks closest to the Van-Hove singularity, where both instabilities are amplified and mutually reinforced [37, 38]. Additionally, narrow magnetic stripes emerge at even-integer chemical potential values. At high values of  $U$  -those that exceed the material’s bandwidth- patches of a charge density wave (CDW) instability appear around regions of the superconducting dome.

The results presented here align with previous studies of the two-dimensional Hubbard model. Dynamical Mean Field Theory (DMFT) has previously captured the coexistence of antiferromagnetic (AFM) and superconducting (SC) order parameters within the same solution across a

range of doping levels (analogous to variations in  $\mu$  in this work) in the weak-coupling regime [39]. A smooth transition between these two phases has also been reported [39]. However, the FRG treatment of the 2D 1NN Hubbard model has not been able to capture certain key features of the Cuprate phase diagram—namely, the Mott insulating phase and the emergence of the pseudogap that have been found in other studies of the 2D Hubbard model [40, 41].

### 5.1.1 Superconductivity in the 1NN Model

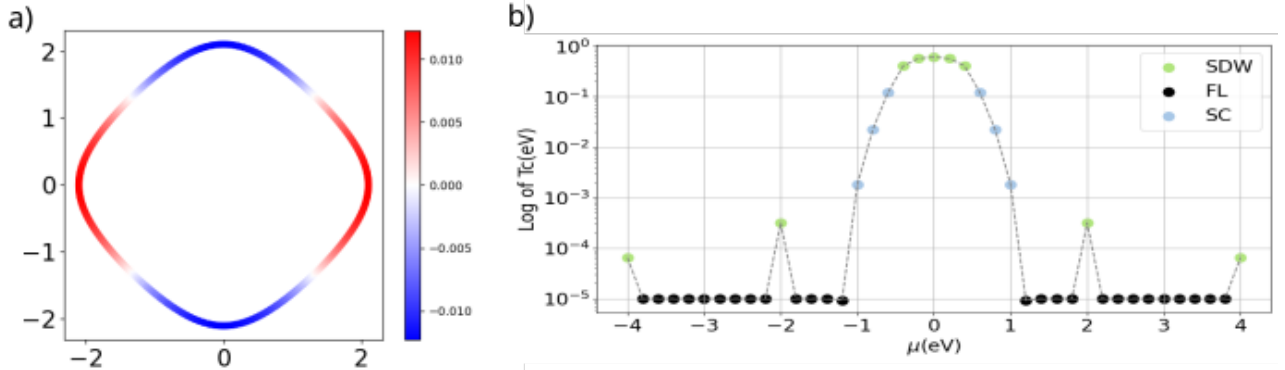


Figure 7: **Superconductivity in the 1NN model:** Panel a) Superconducting order parameter projected on Fermi Surface at  $\mu = 1.00$  eV, for  $U = 7.00$  eV. The order parameter is antisymmetric about a 90-degree rotation and hence it exhibits d-wave symmetry. In particular, it is  $d_{x^2-y^2}$  symmetric. Panel b) Transition temperature ( $T_c$ ) plotted on a logarithmic scale as a function of chemical potential ( $\mu$ ) for  $U = 7.00$  eV, showing a smooth transition between SC and SDW regions.  $T_c$  is enhanced closest to the magnetic instability. Although both plots are shown only specific for certain values of  $U$  and  $\mu$ , the results they display hold for the entirety of the superconducting region of the phase diagram in Fig.6.

Recent findings have claimed that the 1NN 2D Hubbard model does not have a superconducting ground state [42]. Whilst the model in Ref. [42] is the same as the 1NN model explored in this section, the paper's analysis is conducted in a slightly different framework than the one used in this project: using DMRG [43] at moderate-to-strong coupling and for values of  $U$  between 6-8 eV (*the regime relevant to the Cuprates*). The lack of superconductivity in their findings is attributed to a lack of competition between the magnetic and superconducting phases. Here, in the weak-coupling framework, both competition between magnetism and superconductivity and a stabilised superconducting region is found. The superconducting order parameter in this stable region is plotted on top of the Fermi-Surface for the first BZ (Fig.7a). The sign of the order parameter changes with respect to a 90-degree rotation and therefore one concludes that the bulk superconducting region is d-wave symmetric. This is in agreement with what is expected from the Cuprate superconductors [44].

After plotting the critical temperature ( $T_c$ ) as a function of chemical potential ( $\mu$ ) for a constant Coulomb repulsion ( $U$ ), one observes that the superconducting critical temperature is maximized closest to the magnetic instability (Fig.7b). This is in agreement with the idea that competition



between instabilities enhances the transition temperature [45,46]. Moreover, the magnitude of the Coulomb repulsion and  $T_c$  are positively correlated, as is to be expected from the assumed pairing mechanism (See Eq.3).

### 5.1.2 Magnetic stripes in the 1NN Model

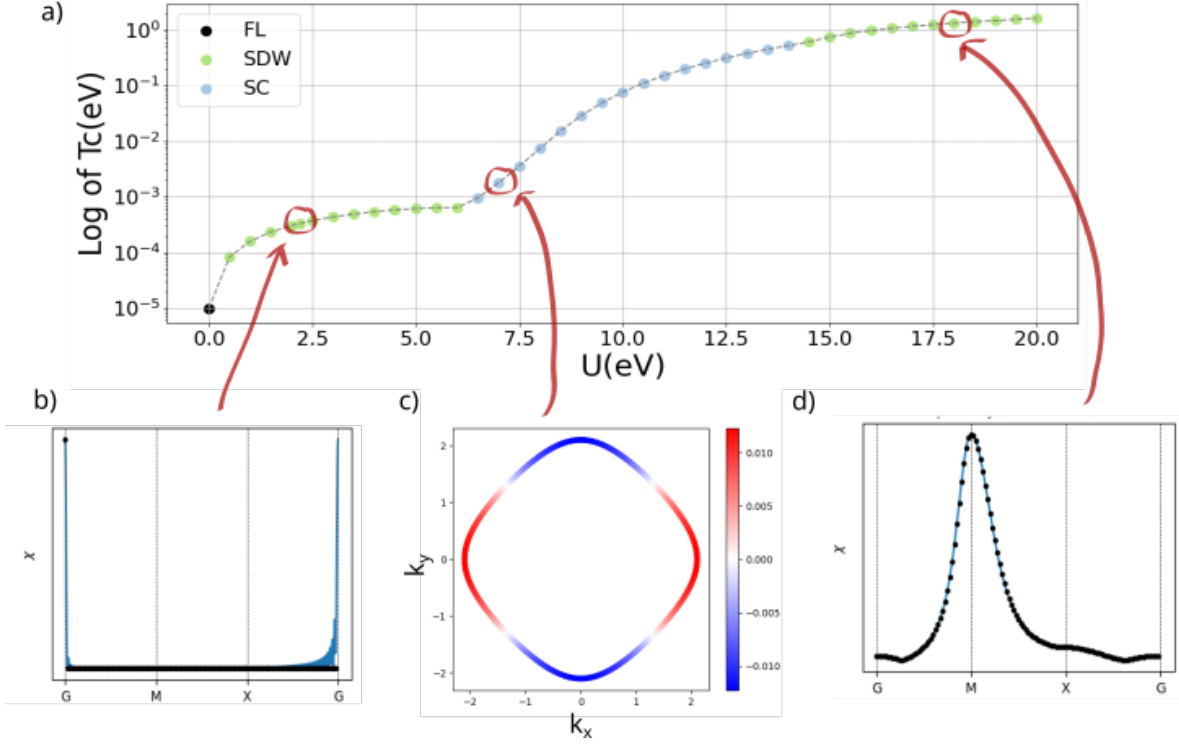


Figure 8: **Magnetic stripe in the 1NN model for doping at  $\frac{1}{8}$  of the bandwidth:** Panel a) Transition temperature plotted in a logarithmic scale as a function of Coulomb repulsion ( $U$ ) along the Magnetic stripe at  $\mu = 1$  eV. Panel b) Magnetic susceptibility along high symmetry path for  $U = 2.00$  eV. Panel c) Plot of the Superconducting order parameter projected on top of the Fermi-surface of the 1NN model for  $U = 7.00$  eV and  $\mu = 1.00$  eV. Panel d) Magnetic susceptibility along high symmetry path for  $U = 18.00$  eV. The plots show the susceptibility as a function of  $q$  for both magnetic regions. The Ferromagnetic SDW is suppressed by a superconducting phase at  $U \approx 6.00$  eV. At larger values of  $U$ , the SDW phase is recovered but with an Anti-Ferromagnetic ordering instead.

Another distinctive feature of the Cuprates (*and of other unconventional superconductors* [47]) is the emergence of “stripes” in their phase diagram. These are patterns of alternating charge-density and spin density waves [48,49]. In the 1NN model discussed here, these patterns are not observed. However, magnetic regions of interest are found outside the main antiferromagnetic (AFM) dome. The 1NN phase diagram in Fig.6 reveals what will henceforth be referred to as “magnetic stripes” occurring at even integer values of the chemical potential ( $\mu$ ). Most of them are ferromagnetically ordered and evolve to some commensurate nesting vector as the Coulomb repulsion is increased.

The physics becomes particularly interesting at a chemical potential of  $\mu = 1.00\text{eV}$ . In Cuprates, a doping of  $\frac{1}{8}$ th is known as “the magic doping” [50], where stripes emerge and superconductivity is suppressed. In this model, the magical doping corresponds to a chemical potential of  $\pm 1.00\text{eV}$  (which is  $\frac{1}{8}$ th of the bandwidth). At low Coulomb repulsion values, a ferromagnetically ordered spin density wave (SDW) is observed. This SDW is suppressed by a superconducting phase, only to be revived at around  $U \approx 15.00\text{eV}$ , where it becomes antiferromagnetically ordered. The superconducting transition temperature  $T_c$  increases along the stripe (*See Fig.8*). While this behaviour is not the same as the conventional stripes seen in Cuprates, it is fair to conclude that there is still something “magical” about the  $\frac{1}{8}$  filling fraction in the 1NN model presented here.

Before conducting this analysis, the possibility of the stripes being a computational artifact was ruled out. This was done by increasing the  $n_k \times n_{k_f}$  resolution for a single point in the stripe and confirming that the result remained unchanged. Additionally, the appearance of these stripes in other models in this report further confirms this.

## 5.2 Effect of next-nearest neighbour hopping (1NNN model)

In real materials, hopping isn’t limited to nearest neighbours; next-nearest neighbour orbitals can also significantly overlap. This motivates the extension of the previously discussed 1NN model to the next-nearest neighbour hopping 2D Hubbard model in a square lattice (1NNN model). Here, the next-nearest neighbour hopping amplitude is varied from 0-0.75 eV in steps of 0.25 eV. The chemical potential of the models is adjusted to ensure that they are all at half-filling in the undoped case. Introducing next-nearest neighbour hopping changes the electronic structure of the model (*See Fig.9a,b*). This results in notable differences in the correlated phases observed in the phase diagrams in Fig.9c.

As the next-nearest neighbour hopping is increased, the position of the Van-Hove singularity shifts to lower energies (*See Fig.9a*). This increase in  $t'$  also alters the Fermi-surface, which in turn changes the nesting vectors of the models. As a result of both these effects, the SC-SDW-SC sandwich region shifts toward the negative chemical potential regime as  $t'$  increases. The superconducting regions remain (in the most-part) d-wave symmetric and the emergence of magnetic stripes remains observable. Additionally, general trends in the superconducting transition temperature ( $T_c$ ) are also observed: it is maximized closest to the magnetic instability, and it increases as a function of  $U$ .

Several studies have explored the effect of  $t'$  in the 2D Hubbard model, employing both FRG [51] and other alternative methods [52], with a particular focus on using  $t'$  as a means to enhance  $T_c$ . The results presented here take a slightly different approach, aiming to compare the features of the 1NN and 1NNN phase diagrams.

### 5.2.1 Superconductivity in the 1NNN Model

Including a next-nearest neighbour hopping parameter in the 1NN model does not lead to many significant changes in the superconducting properties of the model. The order parameter is predominantly d-wave symmetric and the superconducting temperature ( $T_c$ ) increases with Coulomb

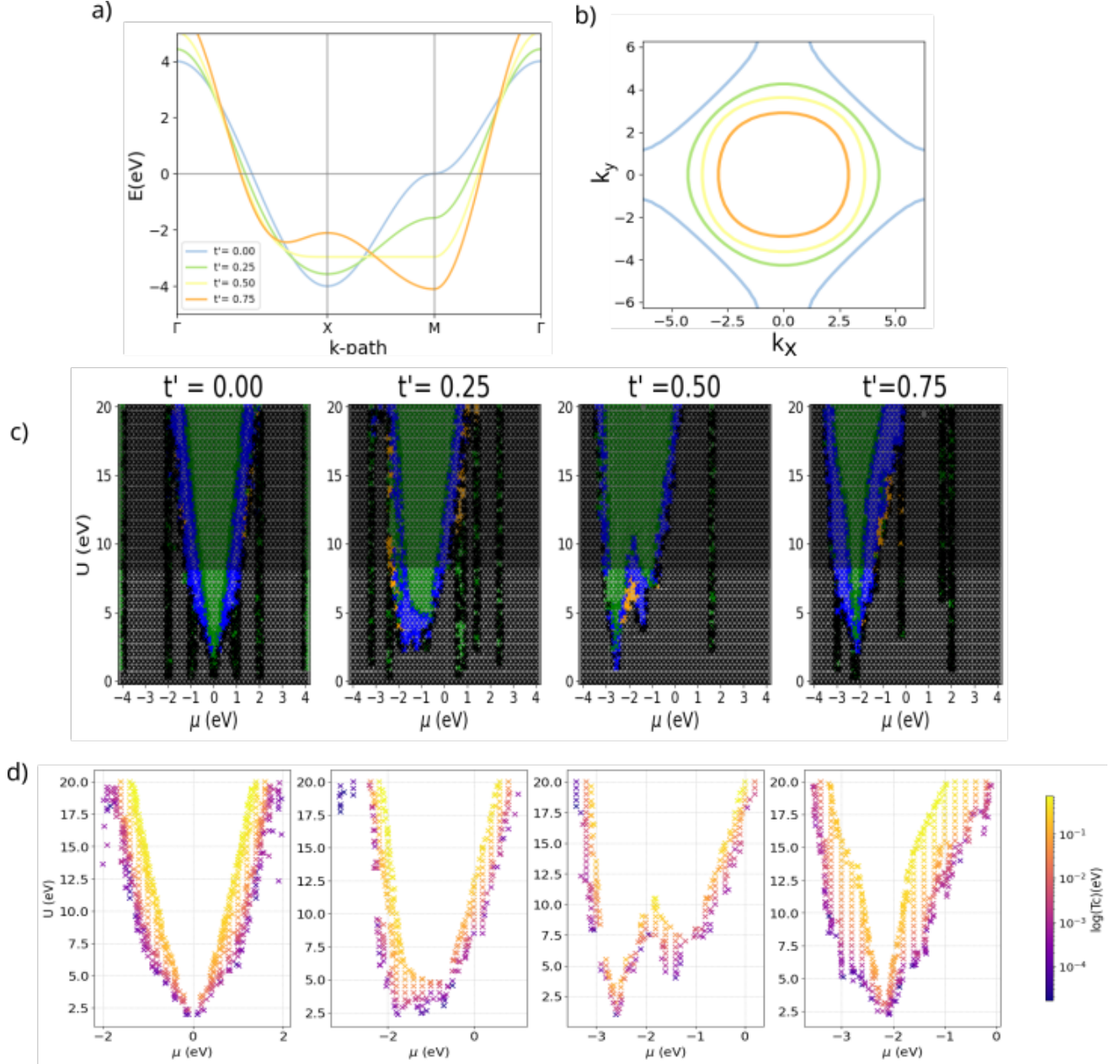


Figure 9: **1NNN model:** Panel a) Single plot of the band structure along high-symmetry path for corresponding values of  $t'$ . Panel b) Single plot of the Fermi surface for all values of  $t'$  considered. Panel c) Phase diagram for the 1NNN model as a function of Coulomb repulsion  $U$  and chemical potential  $\mu$  ( $t = 1\text{eV}$ ,  $n_{k_x n_{k_f}} = 20 \times 5$ ,  $f_f = 4\text{\AA}$ ) for  $t' = 0.00, 0.25, 0.50, 0.75$  eV. A darker mask is applied in the region where results become unphysical. Panel d) Transition temperature for the superconducting region (plotted in a logarithmic scale).

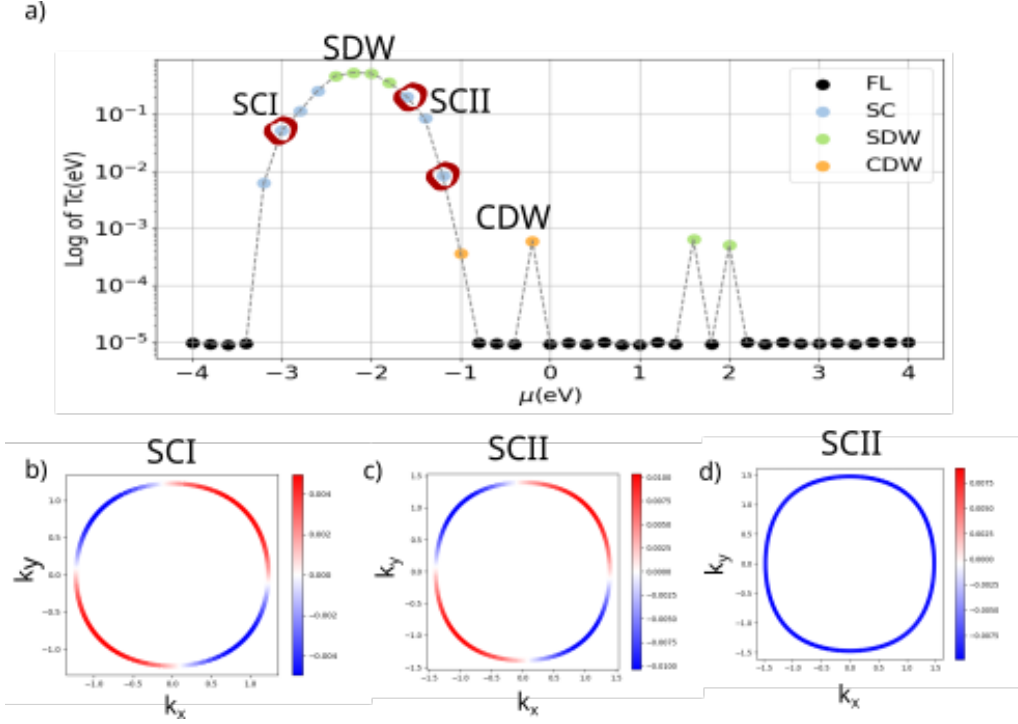


Figure 10: **Change in the superconducting order parameter in the  $t' = 0.75$  eV 1NNN model:** Panel a) Critical temperature plotted in a Logarithmic scale as a function of chemical potential  $\mu$  for  $U = 11.50$  eV. The lower panel shows the magnitude of the superconducting order parameter plotted on top of the Fermi surface for  $U = 11.50$  eV and  $\mu = -3.0$  eV,  $-1.6$  eV and  $-1.2$  eV. These are shown in Panels b) c) and d) respectively.

repulsion. Proximity to a Magnetic instability further enhances  $T_c$ . Additionally, the same SC-SDW-SC sandwich structure is observed even after breaking particle-hole symmetry, reinforcing the idea that that superconductivity is favoured in the vicinity of a spin density wave (SDW) instability.

There are important differences between the superconducting regions in the 1NN and 1NNN model. Whilst the superconducting order parameter remains mostly d-wave symmetric in the 1NNN model, it is a different type of d-wave symmetry than the one observed in the 1NN model. The 1NN model exhibits a  $d_{x^2-y^2}$  symmetry; the 1NNN model exhibits a  $d_{xy}$  symmetry [53]. The only difference between these two types of d-wave superconductivity the plane around which the order parameter is sign antisymmetric (*For direct comparison see Figs 7c and 10b,c*). Moreover,  $t' \neq 0$ , charge density wave (CDW) patches appear neighbouring some superconducting regions. Specifically, when  $\frac{t'}{t} = 0.75$ , and for Coulomb repulsion between 8 and 11eV, the superconducting order parameter undergoes a more significant change. Along these horizontal cuts there is a SCI-SDW-SCII-CDW transition (*See Fig.10*). The Superconducting order parameter is always d-wave symmetric in the SCI region and for most of the SCII region, but it abruptly transitions to s-wave symmetric in the vicinity of the CDW region (*See Fig.10*). This behaviour is also observed in the SC regions that neighbour CDW regions for the  $t' = 0.25, 0.50eV$  models. To confirm whether this represents a physical phase transition, one would expect to experimentally observe a discontinuity as a result of an additional symmetry breaking when the order parameter shifts from s-wave to d-wave symmetry.

### 5.2.2 Magnetic stripes in the 1NNN model

The presence of magnetic stripes is another common feature shared by the 1NN and 1NNN models, further supporting their physical origin. A summary of all the stripes and their respective nesting vectors is provided in Appendix A. The locations of these stripes suggest that their formation is a consequence of strong nesting at specific chemical potential values. Notably, the stripe at  $\mu = 1eV$  in the 1NN model is the only example found where a strong competition between superconductivity and magnetism results in a change of Spin density wave (SDW) ordering.

While the transition from a Fermi liquid phase to any of the superconducting (SC), spin density wave (SDW), or charge density wave (CDW) phases is quite abrupt, the critical temperature evolves more smoothly for stripes where there is a strong competition between SC and SDW/CDW instabilities (*see Fig.11*). This is consistent with the discussion in Section 5.1.2. When  $\frac{t'}{t} = 0.50$ , a magnetic double dome emerges, becoming more pronounced as the Coulomb repulsion increases. This is the pattern one might expect in the superconducting region, as observed in Cuprates [54]. However, this trend is only observed in this particular model and phase.

### 5.2.3 Continuous variation of next-nearest neighbour hopping

Section 5.1 discusses the idea that the location of the Van Hove singularity is strongly related to the location of the area in the phase diagram where the interplay between superconductivity and magnetism is most pronounced. In order to further support this, the critical temperature is

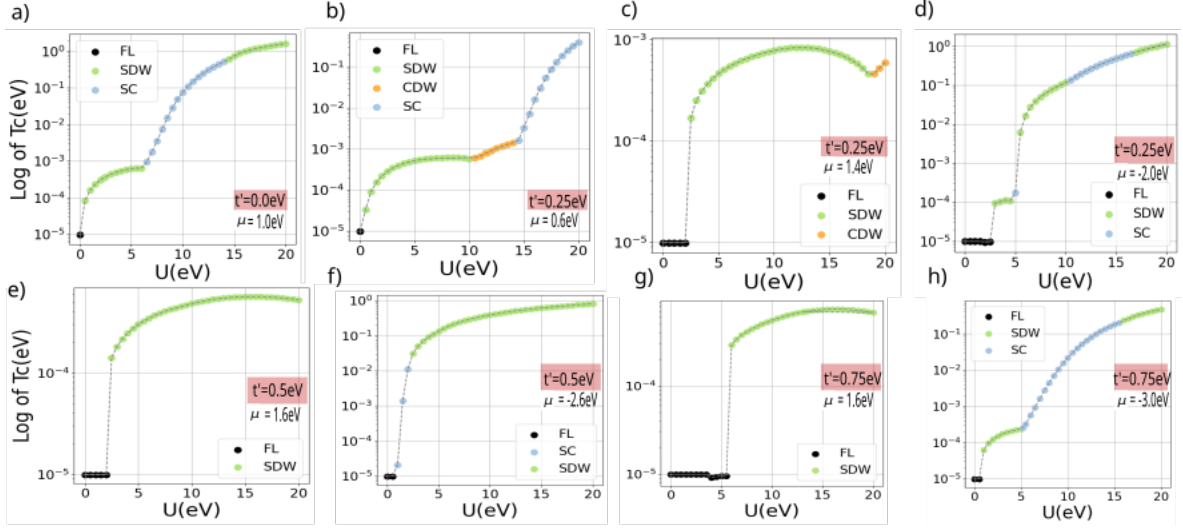


Figure 11:  $T_c$  as a function of Coulomb repulsion for a selection of stripes in the 1NNN model:  $T_c$  plotted in a logarithmic scale for stripes at: Panel a)  $t' = 0.00\text{eV}$ ,  $\mu=1.00\text{eV}$ , b)  $t' = 0.25\text{eV}$ ,  $\mu=0.60\text{eV}$ , c)  $t' = 0.25\text{eV}$ ,  $\mu=1.40\text{eV}$ , d)  $t' = 0.25\text{eV}$ ,  $\mu=-2.00\text{eV}$ , e)  $t' = 0.50\text{eV}$ ,  $\mu=1.60\text{eV}$ , f)  $t' = 0.50\text{eV}$ ,  $\mu=-2.60\text{eV}$ , g)  $t' = 0.75\text{eV}$ ,  $\mu=1.60\text{eV}$ , h)  $t' = 0.75\text{eV}$ ,  $\mu=-3.00\text{eV}$ . Showing abrupt jumps in the critical temperature in FL-(SC,SDW,CDW) phases and a smoother evolution for any SC-SDW/CDW transitions.

plotted as a function of chemical potential  $\mu$  for different values of  $t'$  at  $U=7.00\text{eV}$  (See Fig.12). The magnetic region is pushed towards more negative values of the chemical potential as the value of the next-nearest neighbour hopping parameter is increased (and the van Hove singularity is pushed down in energy). The bulk magnetic region remains anti-ferromagnetically ordered and the SC order parameter is predominantly d-wave symmetric. The exception occurs when  $t'$  is set to  $0.70\text{eV}$ . There, the SC order parameter transitions to s-wave symmetric when it is closest to the boundary with the charge density wave (CDW) phase (as discussed in Section 5.2.1).

### 5.3 Effect of bi-orbital system (1NN2 model)

Model	$t_{3z^2-r^2}^{[1,0,0]}$	$t_{3z^2-r^2}^{[0,1,0]}$	$t_{x^2-y^2}$	$t_{x^2-y^2-3z^2-r^2}^{[1,0,0]}$	$t_{x^2-y^2-3z^2-r^2}^{[0,1,0]}$
	-0.781	-0.719	-0.375	-0.402	-0.310
1NN2MN	on	on	on	off	off
1NN2MY	on	on	on	on	on

Table 1: Nearest-neighbour hopping parameters for 2D two-orbital Hubbard models. First row shows the calculated hopping parameters. These are labelled by a lower and upper index representing the orbital and the direction of hopping respectively. Other rows in the table show which hopping parameters were included in each of the two models from Section 5.3.

Most materials have more than one orbital per atom. This motivates the extension of the 1NN model to a bi-orbital nearest neighbour 2D Hubbard model in a square lattice (1NN2). This

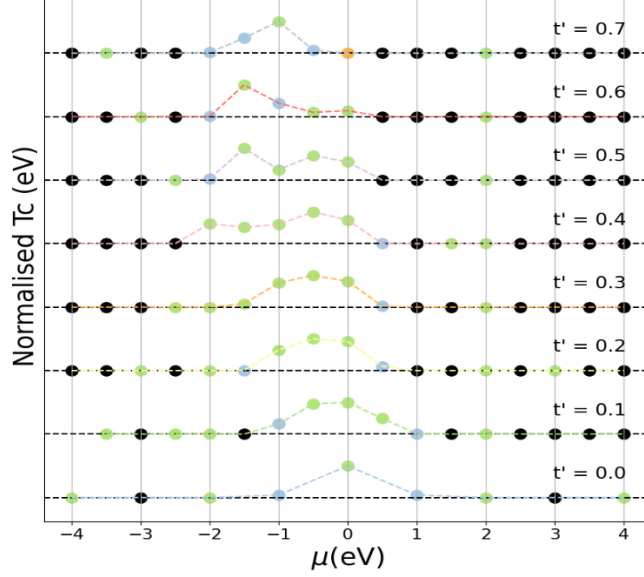


Figure 12: **Continuous variation of  $t'$ :** Normalized  $T_c$  plotted as a function of chemical potential  $\mu$  for several values of  $t'$ .  $T_c$  is normalized separately with respect to the maxima of each plot in order to allow for the clear visualization of the trend as  $\mu$  is varied.

section explores the effect of including two orbitals per site, focusing on the effect of mixing between different orbitals. For such, two different models are investigated: with and without different orbital mixing. To allow for future comparison with existing literature [55], a choice of  $d_{x^2-y^2}$  and  $d_{3z^2-r^2}$  orbitals is made. The respective hopping parameters are determined using the table of inter-atomic matrix elements calculated by J.C. Slater and G.F. Koster [56]. In this calculation, the magnitudes of the  $\sigma, \pi, \delta$  bond strength are approximated to  $\approx 1, 0.5, 0.05eV$  respectively in order to capture their relative values [57–59]. A table summarising the estimated parameters for the models discussed in this section is shown below.

For this discussion the chemical potential is fixed at both the undoped ( $\mu = 0.00eV$ ) and doped ( $\mu = 1.00eV$ ) levels. The choice for the latter value is motivated by the strong interplay between magnetism and superconductivity observed at  $\mu = 1eV$  in the 1NN model. The Coulomb repulsion and Hund's coupling strengths are varied from 1-10eV and 0.1-1.0eV respectively. This section first discusses the 1NN2MY model, where orbital mixing between different orbitals is set to zero, and compares it later with the 1NN2MN model, which includes this orbital mixing.

In the undoped case, the model exhibits an anti-ferromagnetically ordered spin density wave (SDW) ground state for  $U > 3.00eV$ . When the Coulomb repulsion is set to zero, the groundstate transitions to a charge density wave (CDW) with a  $(\pi, \pi)$  nesting vector. Doping the system to a chemical potential of  $\mu = 1.00eV$  suppresses the SDW, and instead, a small superconducting patch emerges in the boundary of the CDW phase (*See Fig.13*). The magnitude of the Hund's coupling has a minor effect in the dominating phase and its transition temperature ( $T_c$ ). The Superconducting regions shown in Fig.13.d exhibit different order parameters. The SC region at  $U=0.0eV$  is s-wave symmetric whilst the SC region at  $U=10.00eV$  is d-wave symmetric. By comparing Figures 13c,d with 13e,f, it can be concluded that the inclusion of different orbital

hopping promotes the emergence of a CDW phase at lower Coulomb repulsion values in the doped case with  $\mu = 1.00eV$ .

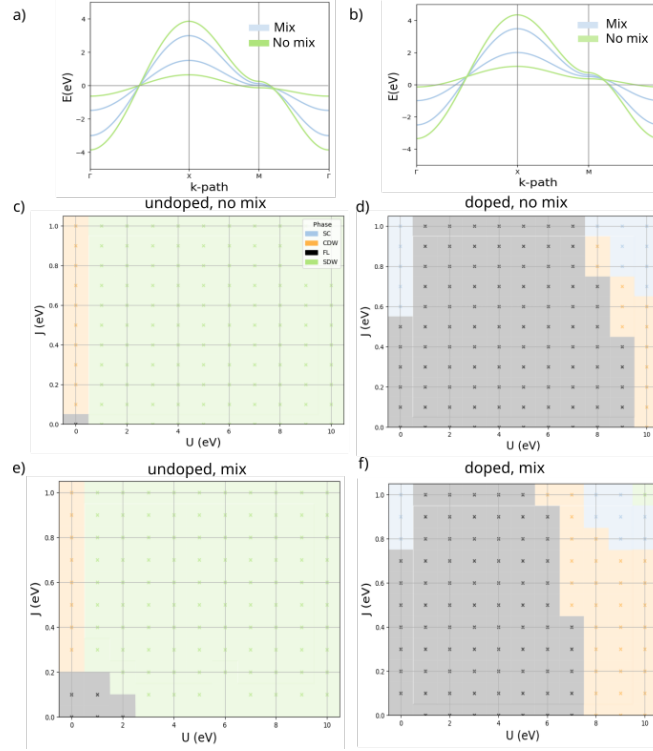


Figure 13: **Phase diagram for the bi-orbital nearest-neighbour Hubbard model on a square lattice** : Phase diagram for the 1NN2 model in terms of the Coulomb repulsion  $U$  and Hund's coupling  $J$  with and without orbital mixing between different orbitals for the undoped and doped cases. Panel a) Band structure for the undoped 1NN2MY/N model. Panel b) Band structure for the 1NN2MY/N model at  $\mu = 1.0eV$ . Panel c) Phase diagram for the undoped 1NN2MY model. Panel d) Phase diagram for the 1NN2MY model at  $\mu = 1.00eV$ . Panel e) Phase diagram for the undoped 1NN2MN model. Panel f) Phase diagram for the 1NN2MN model at  $\mu = 1.00eV$ .



## 6 Conclusion and Outlook

This project aimed to investigate the interplay between Magnetism and Superconductivity in the 2D Hubbard Model at half-filling. The calculations were carried out in the spin-fluctuation mediated superconductivity framework using the two-particle truncated  $TU^2FRG$  scheme in the weak-coupling limit. Although this method fails to capture correlated phases such as Mott-insulating or pseudo-gap phases, it is widely in agreement with previous literature. The results presented here provide a comprehensive study of this model for a uniquely wide range of parameters. A strong competition between an Antiferromagnetically-ordered SDW and d-wave symmetric SC phase is observed. Additionally, several strategies to stabilise and enhance the critical temperature of superconductivity are identified, including increasing the on-site Coulomb repulsion and being near a stabilized SDW region. Narrow magnetic stripes are present, with their ordering changing at the "magical doping" value. The effect of including a next-nearest neighbor hopping parameter is examined in detail. Increasing  $t'$  lowers the Van Hove singularity's energy, shifting the region of prominent SDW-SC interplay towards more negative chemical potentials. A magnetic double dome emerges for a ratio of  $\frac{t'}{t} = 0.50$ . The inclusion of  $t'$  also leads to stable charge density wave (CDW) patches surrounding SC regions, where the SC order parameter transitions from d-wave to s-wave symmetry near these patches. Finally, a preliminary analysis is provided on extending these models to a two-orbital-per-site case. The AFM ground state is suppressed as the model is electronically doped, and the magnitude of Hund's coupling has minimal impact on the observed phases.

Future work could involve a more in-depth analysis of the two-orbital-per-site model, potentially exploring broader ranges of chemical potential and Hund's coupling values. Additionally, extending the study to a bi-layer, two-orbital-per-site Hubbard model would be an intriguing direction. One could also investigate the impact of spin-orbit coupling (SOC) on the results obtained. Such extensions would quickly evolve into a multi-dimensional analysis, offering numerous avenues for exploration. However, a particularly relevant direction would be to progressively increase the complexity of these models to better approximate the behavior of unconventional superconductors, such as lanthanum nickelate. This approach would involve a step-by-step examination of how the critical temperature ( $T_c$ ) and superconducting regions change as model parameters evolve. Ultimately, this could provide valuable insights into the key parameters influencing superconducting phases in unconventional materials.

# References

- [1] Elbio Dagotto. Correlated electrons in high-temperature superconductors. *Reviews of Modern Physics*, 66(3):763, 1994.
- [2] H Kamerlingh Onnes. The superconductivity of mercury. *Comm. Phys. Lab. Univ. Leiden*, 122:124, 1911.
- [3] Theodore H Geballe, Robert H Hammond, and Phillip M Wu. What  $t_c$  tells. *Physica C: Superconductivity and Its Applications*, 514:9–16, 2015.
- [4] J Robert Schrieffer. *Theory of superconductivity*. CRC press, 2018.
- [5] Frank Steglich, J Aarts, CD Bredl, W Lieke, D Meschede, W Franz, and H Schäfer. Superconductivity in the presence of strong pauli paramagnetism: Ce cu 2 si 2. *Physical Review Letters*, 43(25):1892, 1979.
- [6] JE Hirsch, MB Maple, and F Marsiglio. Superconducting materials classes: Introduction and overview, 2015.
- [7] J George Bednorz and K Alex Müller. Possible high  $t_c$  superconductivity in the ba- la- cu-o system. *Zeitschrift für Physik B Condensed Matter*, 64(2):189–193, 1986.
- [8] Christian J Eckhardt, Carsten Honerkamp, Karsten Held, and Anna Kauch. Truncated unity parquet solver. *Physical Review B*, 101(15):155104, 2020.
- [9] Toru Moriya and Kazuo Ueda. Spin fluctuations and high temperature superconductivity. *Advances in Physics*, 49(5):555–606, 2000.
- [10] Gökhan Esirgen and NE Bickers. Fluctuation-exchange theory for general lattice hamiltonians. *Physical Review B*, 55(4):2122, 1997.
- [11] AB Migdal. Interaction between electrons and lattice vibrations in a normal metal. *Sov. Phys. JETP*, 7(6):996–1001, 1958.
- [12] Toru Moriya. Developments of the theory of spin fluctuations and spin fluctuation-induced superconductivity. *Proceedings of the Japan Academy, Series B*, 82(1):1–16, 2006.
- [13] Douglas J Scalapino. The case for dx<sup>2</sup>- y<sup>2</sup> pairing in the cuprate superconductors. *Physics Reports*, 250(6):329–365, 1995.
- [14] Tom Timusk and Bryan Statt. The pseudogap in high-temperature superconductors: an experimental survey. *Reports on Progress in Physics*, 62(1):61, 1999.
- [15] Steven R White, Douglas J Scalapino, Robert L Sugar, EY Loh, James E Gubernatis, and Richard T Scalettar. Numerical study of the two-dimensional hubbard model. *Physical Review B*, 40(1):506, 1989.

- [16] Jorge E Hirsch. Two-dimensional hubbard model: Numerical simulation study. *Physical Review B*, 31(7):4403, 1985.
- [17] Philip W Anderson. “luttinger-liquid” behavior of the normal metallic state of the 2d hubbard model. *Physical review letters*, 64(15):1839, 1990.
- [18] Kai Sun, Zhengcheng Gu, Hosho Katsura, and S Das Sarma. Nearly flatbands with nontrivial topology. *Physical review letters*, 106(23):236803, 2011.
- [19] Alexei Sherman. Hubbard-kanamori model: spectral functions, negative electron compressibility, and susceptibilities. *Physica Scripta*, 95(9):095804, 2020.
- [20] Leo P Kadanoff. More is the same; phase transitions and mean field theories. *Journal of Statistical Physics*, 137:777–797, 2009.
- [21] Naoto Nagaosa. *Quantum field theory in condensed matter physics*. Springer Science & Business Media, 2013.
- [22] Walter Kohn and Lu Jeu Sham. Self-consistent equations including exchange and correlation effects. *Physical review*, 140(4A):A1133, 1965.
- [23] David Bohm and David Pines. A collective description of electron interactions. i. magnetic interactions. *Physical Review*, 82(5):625, 1951.
- [24] Walter Metzner, Manfred Salmhofer, Carsten Honerkamp, Volker Meden, and Kurt Schönhammer. Functional renormalization group approach to correlated fermion systems. *Reviews of Modern Physics*, 84(1):299–352, 2012.
- [25] Julian Lichtenstein, D Sánchez de la Peña, Daniel Rohe, Edoardo Di Napoli, Carsten Honerkamp, and Stefan A Maier. High-performance functional renormalization group calculations for interacting fermions. *Computer Physics Communications*, 213:100–110, 2017.
- [26] Julian Lichtenstein. *Functional renormalization group studies on competing orders in the square lattice*. PhD thesis, Dissertation, RWTH Aachen University, 2018, 2018.
- [27] Masatoshi Imada, Atsushi Fujimori, and Yoshinori Tokura. Metal-insulator transitions. *Reviews of modern physics*, 70(4):1039, 1998.
- [28] Jonas Benedikt Profe. *Functional renormalization group developments for correlations in quantum materials*. PhD thesis, Dissertation, RWTH Aachen University, 2023, 2023.
- [29] J Reiss, D Rohe, and W Metzner. Renormalized mean-field analysis of antiferromagnetism and d-wave superconductivity in the two-dimensional hubbard model. *Physical Review B—Condensed Matter and Materials Physics*, 75(7):075110, 2007.
- [30] Jonas Profe, Dante M Kennes, and Lennart Klebl. diverge implements various exact renormalization group examples. *SciPost Physics Codebases*, page 026, 2024.

- [31] Jacob Beyer, Jonas B Profe, Lennart Klebl, Tilman Schwemmer, Dante M Kennes, Ronny Thomale, Carsten Honerkamp, and Stephan Rachel. Rashba spin-orbit coupling in the square-lattice hubbard model: A truncated-unity functional renormalization group study. *Physical Review B*, 107(12):125115, 2023.
- [32] Cornelia Hille, Fabian B Kugler, Christian J Eckhardt, Yuan-Yao He, Anna Kauch, Carsten Honerkamp, Alessandro Toschi, and Sabine Andergassen. Quantitative functional renormalization group description of the two-dimensional hubbard model. *Physical Review Research*, 2(3):033372, 2020.
- [33] Demetrio Vilardi, Pietro M Bonetti, and Walter Metzner. Dynamical functional renormalization group computation of order parameters and critical temperatures in the two-dimensional hubbard model. *Physical Review B*, 102(24):245128, 2020.
- [34] Steven A Kivelson, Eduardo Fradkin, and Victor J Emery. Electronic liquid-crystal phases of a doped mott insulator. *Nature*, 393(6685):550–553, 1998.
- [35] Eduardo Fradkin, Steven A Kivelson, and John M Tranquada. Colloquium: Theory of intertwined orders in high temperature superconductors. *Reviews of Modern Physics*, 87(2):457–482, 2015.
- [36] Tuomas I Vanhala and Päivi Törmä. Dynamical mean-field theory study of stripe order and d-wave superconductivity in the two-dimensional hubbard model. *Physical Review B*, 97(7):075112, 2018.
- [37] Nobuo Furukawa, TM Rice, and Manfred Salmhofer. Truncation of a two-dimensional fermi surface due to quasiparticle gap formation at the saddle points. *Physical review letters*, 81(15):3195, 1998.
- [38] Carsten Honerkamp and Manfred Salmhofer. Temperature-flow renormalization group and the competition between superconductivity and ferromagnetism. *Physical Review B*, 64(18):184516, 2001.
- [39] Massimo Capone and G Kotliar. Competition between d-wave superconductivity and antiferromagnetism in the two-dimensional hubbard model. *Physical Review B—Condensed Matter and Materials Physics*, 74(5):054513, 2006.
- [40] AA Katanin, A Toschi, and K Held. Comparing pertinent effects of antiferromagnetic fluctuations in the two-and three-dimensional hubbard model. *Physical Review B—Condensed Matter and Materials Physics*, 80(7):075104, 2009.
- [41] Junya Otsuki, Hartmut Hafermann, and Alexander I Lichtenstein. Superconductivity, antiferromagnetism, and phase separation in the two-dimensional hubbard model: A dual-fermion approach. *Physical Review B*, 90(23):235132, 2014.
- [42] Mingpu Qin, Chia-Min Chung, Hao Shi, Ettore Vitali, Claudius Hubig, Ulrich Schollwöck, Steven R White, Shiwei Zhang, and (Simons Collaboration on the Many-Electron Problem).

- Absence of superconductivity in the pure two-dimensional hubbard model. *Physical Review X*, 10(3):031016, 2020.
- [43] Steven R White. Density matrix formulation for quantum renormalization groups. *Physical review letters*, 69(19):2863, 1992.
  - [44] CC Tsuei and JR Kirtley. Pairing symmetry in cuprate superconductors. *Reviews of Modern Physics*, 72(4):969, 2000.
  - [45] M Brian Maple. Interplay between superconductivity and magnetism. *Physica B: Condensed Matter*, 215(1):110–126, 1995.
  - [46] JP Sun, K Matsuura, GZ Ye, Y Mizukami, M Shimozawa, Kazuyuki Matsubayashi, M Yamashita, T Watahige, Shigeru Kasahara, Y Matsuda, et al. Dome-shaped magnetic order competing with high-temperature superconductivity at high pressures in fese. *Nature communications*, 7(1):12146, 2016.
  - [47] Barbara Goss Levi. Are stripes a universal feature of high-t c superconductors? *Physics Today*, 51(6):19–22, 1998.
  - [48] Oron Zachar, SA Kivelson, and VJ Emery. Landau theory of stripe phases in cuprates and nickelates. *Physical Review B*, 57(3):1422, 1998.
  - [49] Matthias Vojta. Lattice symmetry breaking in cuprate superconductors: stripes, nematics, and superconductivity. *Advances in Physics*, 58(6):699–820, 2009.
  - [50] Seiki Komiya, Han-Dong Chen, Shou-Cheng Zhang, and Yoichi Ando. Magic doping fractions for high-temperature superconductors. *Physical review letters*, 94(20):207004, 2005.
  - [51] Christoph Husemann and Walter Metzner. Incommensurate nematic fluctuations in the two-dimensional hubbard model. *Physical Review B—Condensed Matter and Materials Physics*, 86(8):085113, 2012.
  - [52] Rodrigo A Fontenele, Natanael C Costa, Thereza Paiva, and Raimundo R dos Santos. Effects of next-nearest neighbor hopping on the pairing and critical temperatures of the attractive hubbard model on a square lattice. *arXiv preprint arXiv:2503.06753*, 2025.
  - [53] Philip H Butler. *Point group symmetry applications: methods and tables*. Springer Science & Business Media, 2012.
  - [54] Louis Taillefer. Scattering and pairing in cuprate superconductors. *Annu. Rev. Condens. Matter Phys.*, 1(1):51–70, 2010.
  - [55] Hirofumi Sakakibara, Naoya Kitamine, Masayuki Ochi, and Kazuhiko Kuroki. Possible high t c superconductivity in la 3 ni 2 o 7 under high pressure through manifestation of a nearly half-filled bilayer hubbard model. *Physical Review Letters*, 132(10):106002, 2024.
  - [56] John C Slater and George F Koster. Simplified lcao method for the periodic potential problem. *Physical review*, 94(6):1498, 1954.

- [57] Stephen J Blanksby and G Barney Ellison. Bond dissociation energies of organic molecules. *Accounts of chemical research*, 36(4):255–263, 2003.
- [58] John E McGrady. Introduction and general survey of metal–metal bonds. *Molecular Metal-Metal Bonds: Compounds, Synthesis, Properties*, pages 1–22, 2015.
- [59] Andreas Krapp, Matthias Lein, and Gernot Frenking. The strength of the  $\sigma$ -,  $\pi$ -and  $\delta$ -bonds in re 2 cl 8 2-. *Theoretical Chemistry Accounts*, 120:313–320, 2008.

## A Appendix A

t'(eV)	$\mu$ (eV)	Competing with other phase?	Ordering vector	Magnetic ordering
0.00	1.00	Yes (SC)	(0,0)-( $\pi$ , $\pi$ )	FM-AFM
0.00	2.00	No	(0,0)-(0, $\pi$ )	FM-Commensurate
0.25	-3.20	No	(0,0)	FM
0.25	-2.40	No	(0,0)	FM
0.25	-2.00	No	(0,0)-( $\pi$ , $\pi$ )	FM - AFM
0.25	0.60	No	(0,0)	FM
0.25	1.40	Yes (CDW)	(0,0)	FM
0.25	2.40	No	(0,0)	FM
0.50	-2.60	No	(0,0)	FM
0.50	1.60	No	(0,0)	FM
0.75	-3.00	Yes(SC)	(0,0)	FM
0.75	-2.20	Yes(SC)	(0,0)-inc.	FM- Incommensurate
0.75	2.00	No	(0,0).	FM

Table 2: **Survey of stripes in the 1NNN model.** Table summarising the location and magnetic ordering of the Stripes in the 1NNN model .